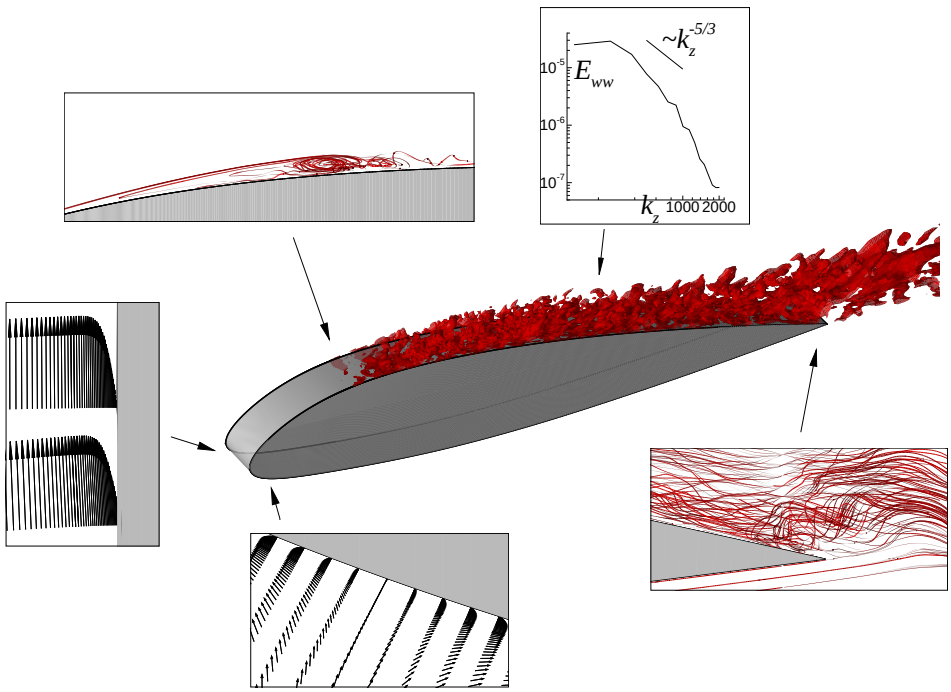

LARGE EDDY SIMULATION OF THE FLOW AROUND A HIGH-LIFT AIRFOIL

SIMON DAHLSTRÖM

Department of Thermo and Fluid Dynamics
CHALMERS UNIVERSITY OF TECHNOLOGY
Göteborg, Sweden 2003

THESIS FOR THE DEGREE OF DOCTOR OF PHILOSOPHY

LARGE EDDY SIMULATION OF THE FLOW AROUND A HIGH-LIFT AIRFOIL

SIMON DAHLSTRÖM

Department of Thermo and Fluid Dynamics
CHALMERS UNIVERSITY OF TECHNOLOGY
Göteborg, Sweden 2003

Large Eddy Simulation of the Flow Around a High-Lift Airfoil
SIMON DAHLSTRÖM
ISBN 91-7291-281-2

Doktorsavhandling vid Chalmers tekniska högskola
Ny serie nr 1963
ISSN 0346-718X

Department of Thermo and Fluid Dynamics
Chalmers University of Technology
SE-412 96 Göteborg, Sweden
Phone: +46 (0)31-772 1400
Fax: +46 (0)31-18 09 76

Cover: Instantaneous contour plot of the spanwise velocity, streamlines, velocity vectors and energy spectra, illustrating the different flow regions around the Aerospatiale A-profile.

Printed by Chalmers Reproservice in Göteborg, Sweden 2003

LARGE EDDY SIMULATION OF THE FLOW AROUND A HIGH-LIFT AIRFOIL

Simon Dahlström

Department of Thermo and Fluid Dynamics
Chalmers University of Technology
SE-412 96 Göteborg, Sweden

ABSTRACT

The work presented in this thesis concerns the efforts of conducting a Large Eddy Simulation (LES) around an airfoil. The airfoil is close to stall, near maximum lift and the Reynolds number is high. In the flow a transitional separation bubble is present. With the aim of solving the flow around an aeroplane, wing or profile at aeronautical conditions, the meshes become inevitably coarse (even for the Aerospatiale A-profile studied in this thesis) and the near-wall region cannot be resolved. The thesis investigates different ways of modelling the near-wall region: by using wall-functions or by using RANS close to the wall. As a result of using coarse meshes, numerical problems arise in the form of unphysical wiggles. This problem is particularly severe in the airfoil flow with its thin laminar boundary layer. In the thesis a wiggle-detector scheme has been used and other ways of treating the laminar region are investigated (by modifying the SGS-models and the spatial schemes). It is found that the treatment of the laminar region has a major effect on the turbulent boundary layer further downstream. The thesis also discusses the requirements on the resolution when the near-wall region is (or should be) modelled and tries to see the benefits of using a Large Eddy Simulation in such simulations.

Keywords: Large Eddy Simulation, Incompressible Finite Volume, Airfoil, Transition, Mildly Separation, Approximate Wall Boundary Condition, Hybrid RANS/LES.

PREFACE

This thesis is based on the below listed papers. I am the first author in all of them, with the exception of Paper II. In this paper Håkan Nilsson is the first author.

Paper I: S. Dahlström and L. Davidson, ”Large Eddy Simulation of the Flow Around an Aerospatiale A-aerofoil”, *ECCOMAS 2000, European Congress on Computational Methods in Applied Sciences and Engineering*, 11-14 September, Barcelona, Spain, 2000.

Paper II: H. Nilsson, S. Dahlström and L. Davidson,”Parallel Multiblock CFD Computations Applied to Industrial Cases.” *Parallel Computational Fluid Dynamics - Trend and Applications*, Elsevier Science B.V., C.B. Jenssen et al. (eds.), pp. 525-532, 2001.

Paper III: S. Dahlström and L. Davidson, ”Large Eddy Simulation of the Flow Around an Airfoil”, AIAA paper 2001-0425, Reno, NV, 2001.

Paper IV: S. Dahlström and L. Davidson, ”Large Eddy Simulation Applied to a High-Reynolds Flow Around an Airfoil Close to Stall”, AIAA paper 2003-0776, Reno, NV, 2003.

Paper V: S. Dahlström and L. Davidson, ”Hybrid RANS/LES employing Interface Condition with Turbulent Structure”, to be presented at the ICHMT International Symposium on *Turbulence, Heat and Mass Transfer IV*, 12-17 October, Antalya, Turkey, 2003.

Relevant publications not included in this thesis:

Paper VI: S. Dahlström and L. Davidson, ”Contribution by Chalmers in LESFOIL- Large Eddy Simulation of Flow Around a High-Lift Airfoil”, L. Davidson et al. (eds.), Notes on Numerical Fluid Mechanics, Vol. 83, pp. 80-96, Springer, 2003.

Paper VII: S. Dahlström, ”Large Eddy Simulation of the Flow Around a High-Lift Airfoil”, Thesis for the degree of Licentiate of Engineering, *Report 00/5, Dept. of Thermo and Fluid Dynamics, Chalmers University of Technology*, 2000.

Contents

ACKNOWLEDGEMENTS

This work was carried out at the Department of Thermo and Fluid Dynamics at Chalmers University of Technology. I would like to express my gratitude to my supervisor Prof. Lars Davidson, who has been an encouraging support. I would also like to express my gratitude to my colleagues at our department. Especially to Shia-Hui Peng who has been supportive, to Håkan Nilsson for helping me with parallelisation issues and also to Lars-Erik Erikson for providing me with his mesh generator.

The interesting and stimulating discussions that always arose on the LESFOIL meetings are gratefully acknowledged and my thanks goes to all the people involved in that project. Especially to Chris Mellen and Lionel Temmerman for among other things interesting e-mail correspondence.

The work was financed by the LESFOIL and the FLOMANIA projects. The LESFOIL project (LES of Flow Around a High-Lift Airfoil), a Brite-Euram programme (Project No. BRPR-CT97-0565), was a collaboration between Alenia, CERFACS, Chalmers University, Dassault, Fluent Europe Ltd, Karlsruhe University, ONERA, The University of Surrey and QMW/UMIST. The FLOMANIA project (Flow Physics Modelling - An Integrated Approach) is a collaboration between Alenia, AEA, Bombardier, Dassault, EADS-CASA, EADS-Military Aircraft, EDF, NUMECA, DLR, FOI, IMFT, ONERA, Chalmers University, Imperial College, TU Berlin, UMIST and St. Petersburg State University. The project is funded by the European Union and administrated by the CEC, Research Directorate-General, Growth Programme, under Contract No. G4RD-CT2001-00613.

Finally, computer time at the IBM SP machine at PDC, Stockholm is acknowledged.

1 INTRODUCTION

The focus of the work presented in this thesis has been to apply Large Eddy Simulation (LES) on a high-Reynolds flow around a profile close to stall. The work has been a part of the LESFOIL project and is presently a part of the FLOMANIA project, where besides the airfoil flow, also the flow in an asymmetric plane diffuser is studied.

In LES the large-scale eddies are resolved and the small scales are modelled. The uncertainty of the modelling is reduced when the *important* large scales are resolved. This is the case with wall-resolved large-eddy simulations, where the important near-wall structures are partly resolved. These structures are large compared to the small-scale turbulence in this region, however, they are not large, compared to other length scales in the outer part of a boundary layer and wall-resolved simulations are often not a feasible alternative because they are far too expensive to perform.

Instead, in the high-Reynolds flow around the airfoil, the minimum requirements in order to conduct an LES are investigated. In this approach the near-wall region is to be modelled and the question is: what resolution is required in the region outside the near-wall region? The minimum requirement is to resolve large flow structures such as boundary layers, separation bubbles etc., with a sufficient amount of nodes. Different types of flow structures are shown in Chapter 2 and different approaches to solve these flows are described in this chapter.

The value of having a good LES resolution in the off-near-wall region and to see the benefits of using this LES approach is investigated. In LES the filtered (time-dependent) Navier-Stokes equations are solved. LES thus gives information about the transients of the flow and the simulations give a physical representation of the flow as the time progresses. In Chapter 4 this feature of LES is used to visualise the different flow regions around the Aerospatiale A-profile.

A major part of the work on the airfoil regards how to achieve an LES at this high Reynolds number. This is discussed in Chapter 5 and regards 1) the use of a wiggle detector 2) having a sufficient resolution in the off-near-wall region and 3) having knowledge of the different flow regions around the profile. Given that there is no a priori knowledge of the flow, this can only be gained in an iterative manner discussed in this chapter. The chapter tries to highlight the considerations and

requirements in order to get a physically qualitatively good LES. To get quantitatively better results, especially two issues are discussed:

- Regarding the aerofoil, there is an uncertainty about how to treat the laminar region, which seems to be crucial to get the transitional bubble at the correct location.
- The other issue regards near-wall treatment. In Chapter 6 different near-wall treatments are discussed: wall-functions and the use of RANS close to the wall. A method using interface conditions with turbulent structures at the interface between the LES and RANS region is presented.

What are the perspectives of LES? In Chapter 7 the cost and future for LES are estimated for different LES approaches.

2 RESOLVING AND MODELLING TURBULENCE

There are a range of aspects concerning turbulent flows. The aim with this chapter is partly to highlight the difference between modelling and resolving turbulence and partly to discuss which flow structures that need to be resolved in different approaches, especially focusing on RANS and LES.

Flow Structures

A distinction could be made between two types of flow structures:

- Mean flow structures
- Turbulent flow structures

In both LES and RANS the mean flow structures need to be captured (or resolved). For example when resolving the laminar boundary layer in Fig. 1, the resolution must be sufficiently fine, in the streamwise

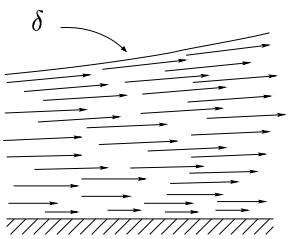

Figure 1: Laminar boundary layer.

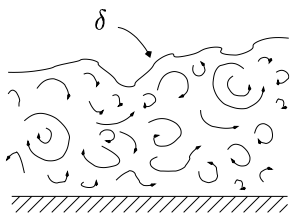

Figure 2: Vortices or eddies in a turbulent boundary layer.

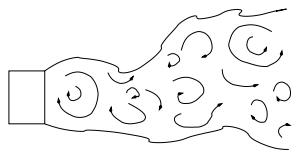

Figure 3: Eddies or turbulent structures in a wake.

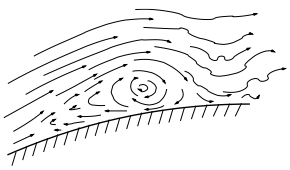

Figure 4: Separation bubble.

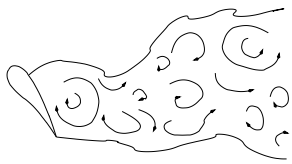

Figure 5: Detached eddies in massively separated flow.

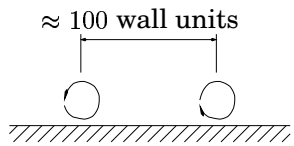

Figure 6: Near-wall streaks.

direction, to capture the increase in the boundary layer thickness. Another example is a separation bubble, either a laminar one (see Fig. 4) or a bubble present in the mean, which needs to be discretized with a sufficient amount of nodes in the streamwise and wall-normal direction.

The turbulent flow structures are modelled altogether in RANS and in LES the important turbulent flow structures are resolved and the less important (smaller scales) are modelled. Here a distinction could be made between two types of important turbulent structures:

- Important energy-containing large eddies away from the wall. Examples are whirls in a turbulent boundary layer, in a wake or in a massively separated flow (Figs. 2, 3 and 5).
- Near-wall structures such as near-wall streaks (see Fig. 6), hairpin vortices, bursting processes, sweeps and ejections.

Near-wall structures

The regions near the wall are the viscous sublayer, the buffer region and the logarithmic region. The viscous sublayer is a thin region extending up to eight wall units away from the wall (1 wall unit $= \nu/u_\tau$). The near-wall streaks are streamwise counter-rotating vortices in this region. They have an approximate spanwise periodicy of 100 wall units and a length of 1000 wall units. These turbulent structures are important, since they interact with the buffer region and are responsible for a major part of the energy production through the *bursting* process [1]. Other mechanisms in the buffer region are *sweeps* (when high-speed fluid from the logarithmic region enters the buffer region) and *ejections* (when low-speed fluid from the buffer region enters the logarithmic region). When talking about the *near-wall region*, it is the region where the above described structures prevail.

Eddies in the off-near-wall region (> 30 *wall units)*

Talking about the *off-near-wall region*, it is the region outside of where the near-wall structures prevail. In a turbulent flow there are eddies (whirls and swirls) of different sizes. The eddies are stochastic, however in the mean, the energy in the eddies of a certain size could be

collected and an energy spectrum could be plotted. In Figs. 7 and 8 typical energy spectra at different Reynolds numbers are shown at a point in the turbulent boundary layer.

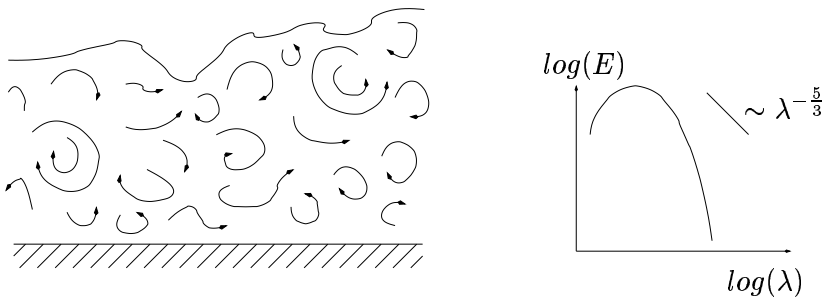

Figure 7: Turbulent boundary layer at low Reynolds number and energy spectrum at a point.

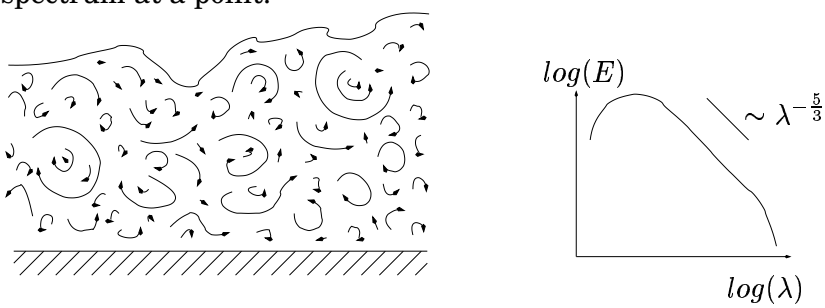

Figure 8: Turbulent boundary layer at high Reynolds number and energy spectrum at a point.

As the scale of the eddies get smaller they get more isotropic, regardless of the anisotropy of the large-scale flow. The assumption that the smallest scales are isotropic is in accordance with Kolmogorov's (1941) universal equilibrium theory, which states that if the Reynolds number is high enough then there exists a range of wave numbers, the *equilibrium range*, where the scales are independent of the large scale flow and depend only on the dissipation rate, ϵ, and the viscosity, ν. The spectrum in Fig. 8 also shows another region, the linear region in the log-log plot, called the *inertial subrange*, where the eddies are also independent of the viscosity. The existence of these regions have been confirmed in experiments and simulations. For example, Saddoughi and Veeravalli [2] have found clear indications of local isotropy in the inertial subrange in their measurements in a high Reynolds turbulent

boundary layer flow.

Numerical Approaches to Solve Turbulent Flows

DNS

In Direct Numerical Simulation, DNS, almost all scales in a flow field are resolved, from the largest scales down to the Kolmogorov length scales. The Kolmogorov scales are the smallest scales in a turbulent flow, with the length scale, η, time scale, τ, and the velocity scale, υ, given by:

$$\eta \equiv \left(\nu^3/\varepsilon\right)^{1/4} \quad \tau \equiv (\nu/\varepsilon)^{1/2} \quad \upsilon \equiv (\nu\varepsilon)^{1/4} \tag{1}$$

The structure of the turbulence becomes finer as the Reynolds number ($Re_\ell = u\ell/\nu$) increases. Thus the DNS resolution has to increase with increasing Reynolds number. If the largest scales in a flow are of the size ℓ, the number of nodes required in a DNS, in one direction, is proportional to ℓ/η ($\sim Re_\ell^{3/4}$). The total number of nodes thus scales like $Re_\ell^{9/4}$, and the numerical problem becomes too expensive at a relatively low Reynolds number. Further, if walls are present, the near-wall structures need to be resolved leading to an even stronger dependence on the Reynolds number (see Chapter 7).

Wall-resolved LES

In a wall-resolved LES, the distance from the wall to the first node should be at least less than two wall units. Although the velocity profile in the viscous sublayer ($y^+ < 5 - 8$) is linear in the mean, instantaneously this need not be the case and y^+ must be less than two in order to resolve the instantaneous velocity gradient close to the wall. Also the near-wall structures described above need to be sufficiently resolved. They can be captured if the sizes of the cells closest to the wall are within the range of $50 < \Delta x^+ < 150$, $y_1^+ < 2$ and $15 < \Delta z^+ < 40$ [3].

Coarse LES

The fact that the small scales are more isotropic makes them easier to model and assuming that the inertial range dynamics (and the local

isotropy) sets in independently of the Reynolds number relative to the largest scale in the flow, ℓ, then the required resolution in an LES is also independent of the Reynolds number. However, what need to be stressed, is that the largest scale in a flow could be very small. Looking at the different types of flows shown in Figs. 1-6 once again, both the laminar and the turbulent boundary layers could be very thin and so could the separation bubble.

RANS

In RANS the time-averaged Navier-Stokes equations are solved. The governing equations for RANS looks exactly the same as the ones for LES (see Appendix). However the eddy viscosity term plays a completely different role in the two approaches. In the RANS approach all turbulence is modelled and the eddy viscosity locks the flow. The problem is to find a model that is able to model the turbulence in different types of flows and often the constants need adjusting, depending on type of flow.

DES

The LES idea seems to work well in the case of turbulence with inertial range dynamics and where the largest scales in the flow are easily resolved. This is the case for the detached eddies in airfoil flows at stall (see Fig. 5). In the Detached Eddy Simulation (DES) approach, RANS is used near walls and LES in the detached part of the flow (see e.g. [4–7]).

Hybrid RANS/LES

In hybrid RANS/LES, RANS is used close to walls in order to model the near-wall-region flow. The requirements on the resolution is less severe for RANS compared to LES, since the structures only need to be resolved in the mean. In the RANS region the eddy viscosity models all turbulence. LES is used in the region outside the near-wall region. Here the eddy viscosity decreases, modelling only the unresolved stresses, and the resolved stresses increases. The main problem with hybrid RANS/LES is how the matching between these completely different approaches should be done.

3 AIRFOIL FLOW

Background

Figure 9 shows the Aerospatiale A-profile and the specific case that has been studied in the LESFOIL project [8] and now also included as a test case in the FLOMANIA project.

Some nomenclature for the airfoil now follows. The front part of the airfoil is called the leading edge and the rear part is called the trailing edge. The chord of the airfoil, c, is the distance from the leading to the trailing edge. The upper side of an airfoil is called the suction side and the lower the pressure side. The angle of attack, α, is the angle between the chord line and the freestream velocity, U_∞.

Measurements of this flow has been carried out in two wind tunnels, the F1 and F2 wind tunnels at Onera [9]. A range of flow data was collected in these experiments, at different Reynolds numbers and at different angels of attacks. However, the case studied in the LESFOIL project, was the $13.3°$-case and based on the freestream velocity and the chord of the airfoil the Reynolds number, $Re_c = U_\infty c/\nu$, is equal to 2 million. The flow is subsonic with a freestream Mach number of 0.15. This is exactly one of the set-ups carried out in the F2 wind tunnel. In the F1 wind tunnel, the nearest set-ups were incidences equal to 13.1 and 14.1 and Reynolds numbers of 2.07 and 3.13 million. In both experiments the boundary layer was tripped at 30 % of the chord on the pressure side.

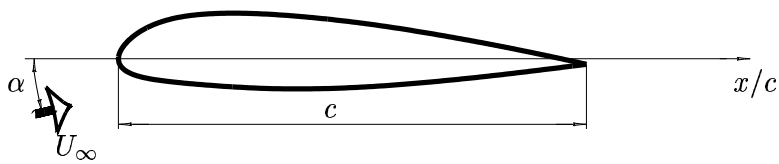

Figure 9: Airfoil case.

Near maximum lift and close to stall

In Fig. 10 experimental results of the lift and drag versus the angle of attack are shown. The dashed line marks the $13.3°$-case and we see that the flow is near maximum lift and the airfoil is close to stall. The

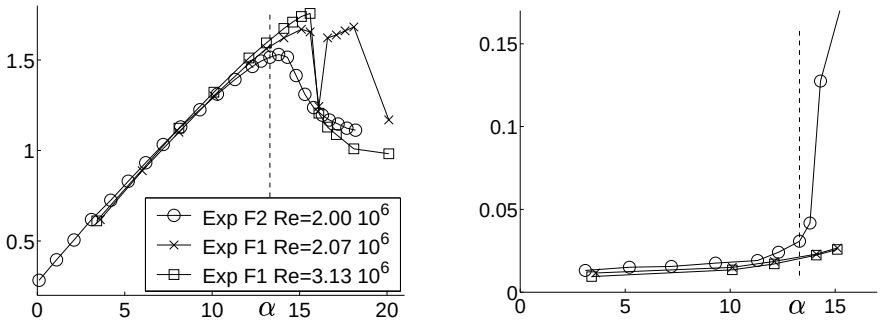

Figure 10: Lift and drag coefficients versus the angle of attack.

flow separates at about 82.5 % of the chord in the F2 experiments. The separation is weaker in the experiment in the F1 tunnel, where it occurs at approximately 95 % of the chord. That the flow is closer to stall in the F2 wind-tunnel measurements is also seen in Fig. 10. A too large blockage in the experimental setup in the F2 wind tunnel is probably the main reason for the difference between the two experiments [9].

Take-Off and Landing Conditions

In Fig. 11 the set-up condition for the Aerospatiale A-profile at $Ma = 0.15$ and $Re = 2 \cdot 10^6$ is compared to different conditions for some aeroplanes. The set-up condition is in the region where stall, take-off and landing occurs for a small aeroplane, such as the Cessna (it differs a factor of approximately 2). The stall velocity, V_s, the velocity at which stall occurs, is the minimum velocity during a flight. The take-off and landing velocities are often related to the stall velocity, as $1.2V_s$ and $1.3V_s$, respectively. Thus the Reynolds number at take-off and landing is only 20-30 % higher than at stall. Comparing with a large air-craft, such as Boeing 747, the Reynolds number is almost 25 times higher than in the Aerospatiale case, although still in the region where incompressible methods (such as those used in the present thesis) apply. The required resolution at this much higher Reynolds number is estimated in Chapter 7 for smooth 2D and 3D wings.

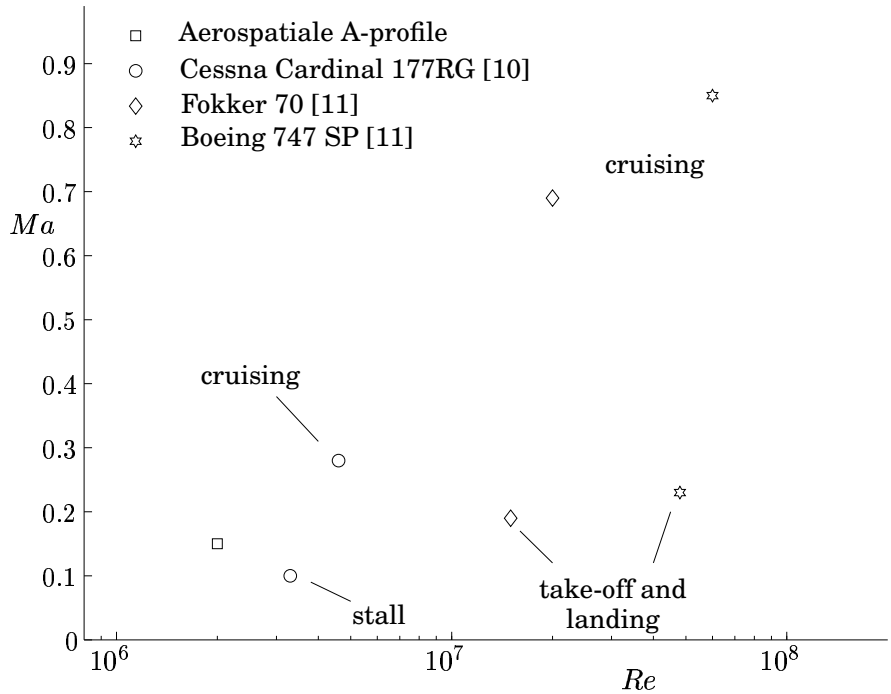

Figure 11: Take-off, landing, stall and cruising conditions for some aeroplanes and the set-up condition for the Aerospatiale A-profile.

Different Numerical Approaches

The flow around the Aerospatiale A-airfoil has been the subject of extensive studies. Different CFD codes (steady and unsteady RANS, compressible and incompressible methods) were validated in the EUROVAL project [12] and in the ECARP project [13] on this particular single-element airfoil. It was found that few RANS models are capable of handling this flow problem, mainly because of the lack of curvature effects in the eddy-viscosity models. The second-moment closures (which do take into account curvature effects) produced the best results [14–16].

Large Eddy Simulation (LES) of flows around airfoils have been conducted prior to the LESFOIL project, e.g. in a study on the NACA 4412 profile [17], the present A-profile [18] and in extensive studies including compressible flow [19]. A new study on the Aerospatiale A-

profile is found in Ref. [20].

4 USING LES TO VISUALISE AIRFOIL FLOW

Because of the shape of the airfoil and the angle of attack the flow streams faster on the suction side of the profile. Bernouli's equation states that this means low pressure and the opposite on the pressure side: lower velocity and an increase in the pressure. This is the mechanism that make the airfoil lift. In Fig. 12 we see the pressure distribution around the A-profile. Blue colour is low pressure and red is high. Almost all over the suction side the pressure is lower than the freestream pressure, especially in the region around the leading edge, where there is a pressure peak. At approximately 20 % of the chord and downstream the pressure fluctuates: the pressure decreases or increases locally resulting in eddies or swirls in the flow. Here in this region the flow is turbulent.

Figure 12: Pressure contours.

In Fig. 13 the stagnation point region and a part of the very thin laminar boundary layer are shown. On the suction side, there is a peak in the pressure gradient near the leading edge. The favourable pressure gradient accelerates the flow around the leading edge. In Fig. 14 streamlines are shown in the transitional region. In the left part of the figure the streamline does not fluctuate, i.e. the boundary layer is laminar and then a separation bubble is formed. Inside of this bubble, the streamlines look more chaotic and a transition is taking place. When the flow reattaches the streamline fluctuates and the boundary layer is turbulent. In Fig. 15 the axis do not have the same scaling in order to get a better picture of the transitional bubble and in Fig. 16

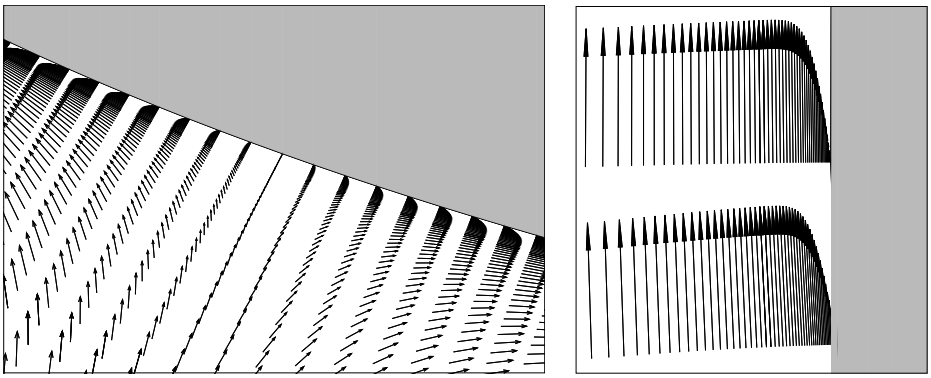

Figure 13: The stagnation point region and the laminar boundary layer at the leading edge.

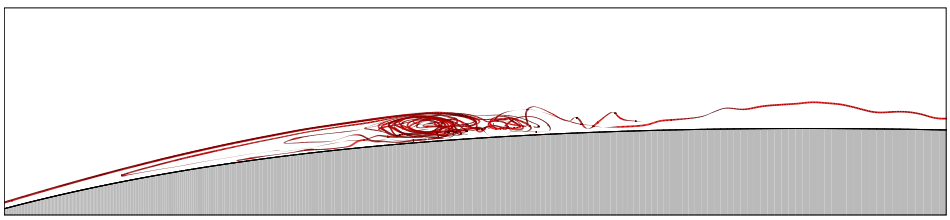

Figure 14: Side view of the transitional bubble.

the transitional bubble is seen in a 3D view.

The turbulent boundary layer shown in Fig. 17 grows under the influence of an adverse pressure gradient. In Fig. 18 a rear view of streamlines illustrates the turbulent boundary layer and the eddies (or swirls) that are present at an instant in this region. The fluctuations get more intense in the turbulent boundary layer in the region close to the airfoil. Figure 19 shows a side view of streamlines in the trailing edge region and a small separation bubble is seen. When the angle of attack increases, this bubble gets larger and finally the airfoil stalls and looses its lift.

Finally in Fig. 20 a long distance side view of the profile and the turbulence is shown. The turbulent boundary layer along the suction side is clearly seen and downstream of the trailing edge the wake extends far downstream of the profile.

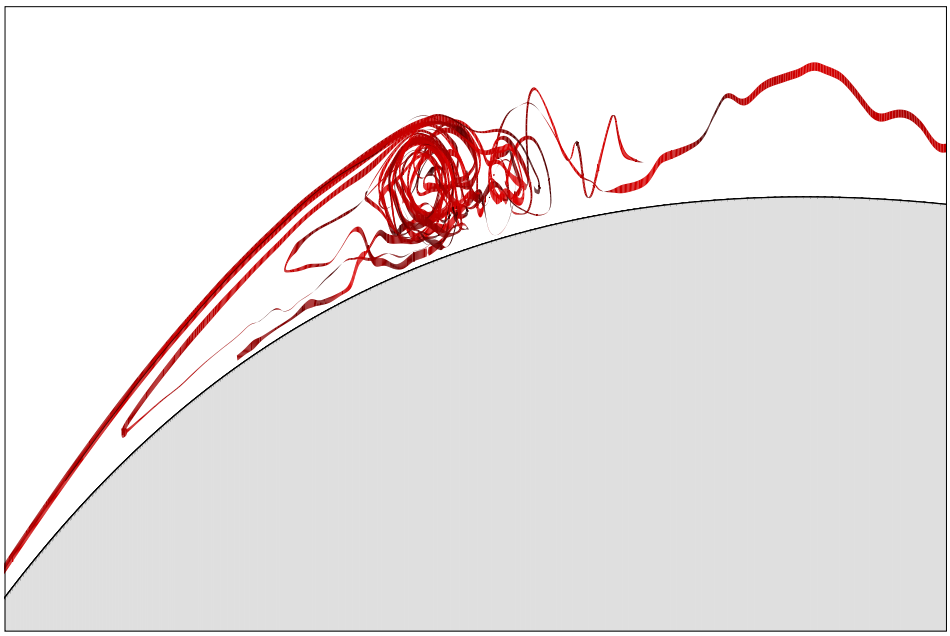

Figure 15: Side view of the transitional bubble (different scaling on the axes).

Figure 16: 3D view of streamlines showing the transitional separation bubble.

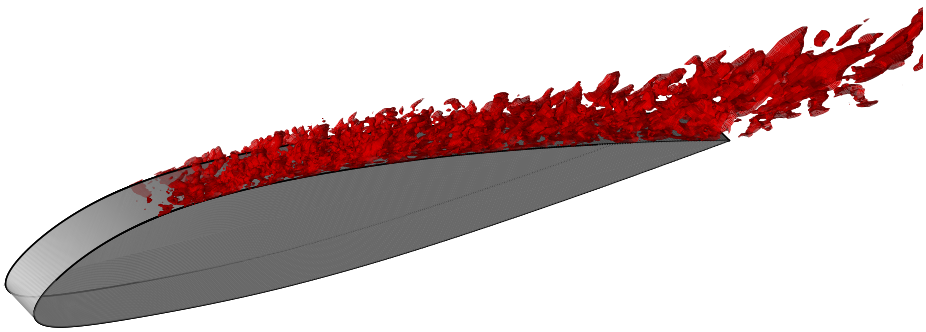

Figure 17: Instantaneous contour plot of the spanwise velocity.

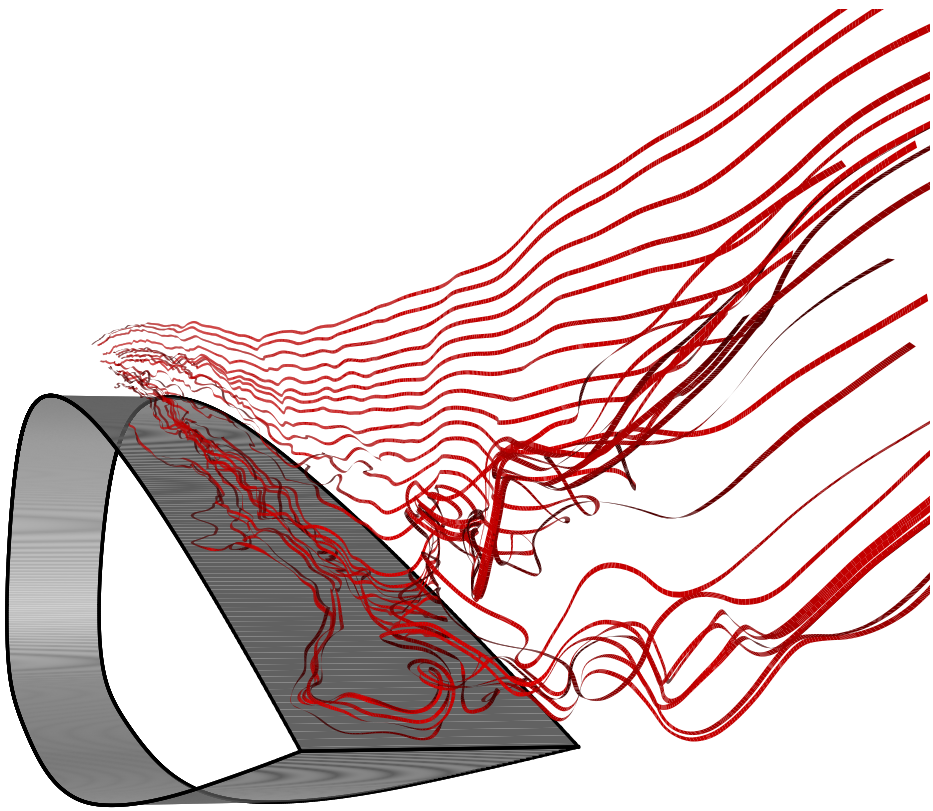

Figure 18: Rear view of streamlines in the turbulent boundary layer.

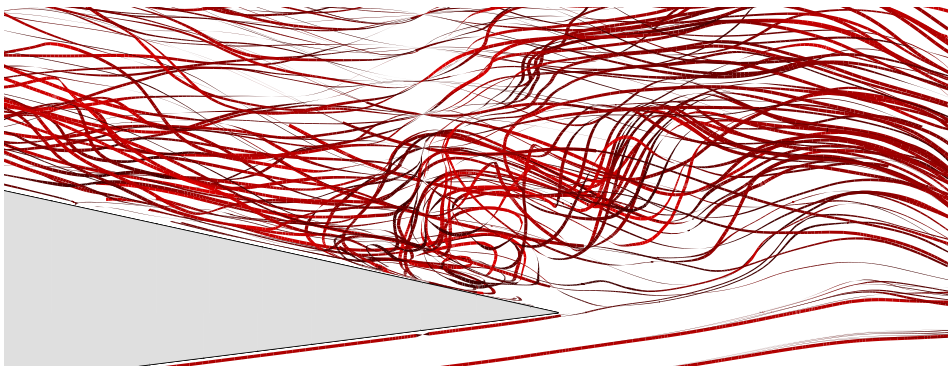

Figure 19: Side view of streamlines near trailing edge.

Figure 20: Side view of the profile and wake (w-contour levels of 0.2 % of the freestream velocity.

5 NUMERICAL ISSUES AT HIGH-REYNOLDS FLOWS

Resolution Iteration Process

In the beginning of the LESFOIL project a mesh, *the Chalmers mesh*, was constructed. It consists of 720×65 grid nodes in the streamwise and wall-normal direction. This will be referred to as the first, initial or coarse mesh in this chapter. From the results of the computations on the initial mesh a range of conclusions could be drawn. All conclusions below but one could be deduced from these initial computations.

- The resolution does not capture all of the large eddies in the turbulent boundary layer until the resolution approaches $\Delta x^+ \approx \Delta z^+ \approx 200$ or $N_x \approx N_z \approx 8$ (defined below).
- The possible existence of a laminar separation bubble.
- Poor resolution of the laminar boundary layer.
- Unphysical oscillations are present $\Rightarrow$ finer resolution or more dissipative scheme needed.
- When the trailing edge separation bubble appears it is very thin.

It is difficult to note the last point from the results and knowledge about the experiments or knowledge about trailing-edge separation bubbles are necessary. A new mesh, *the Chalmers II mesh*, was constructed in order to take into account the above considerations. This mesh will be referred to as the second-iteration mesh or the finer mesh in this chapter. In Table 1 data on the two meshes are shown.

Resolving the flow in the off-near-wall region

None of the meshes have been designed to resolve the near-wall region. The aim with the second mesh, the Chalmers II mesh, was to resolve the flow in the region outside the near-wall region (outside the region where the near-wall structures, described in Chapter 2 prevail). From the first mesh we could see that the flow was sufficiently resolved when the resolution was less than approximately 200 wall units or $N_x \approx N_z \approx 8$. Here N_x and N_z are the number of nodes per boundary

Mesh	**Chalmers mesh**	**Chalmers II mesh**
# of grid nodes:	720×65	1393×127
# of nodes along the wake:	109	110
# of nodes on the pressure side:	201	426
# of nodes on the suction side:	302	748
Length of the cell at the leading edge:	$0.0010c$	$0.0010c$
Height of the cell at the leading edge:	$0.00026c$	$5.1 \cdot 10^{-6}c$
Length of the cell at the trailing edge:	$0.0050c$	$0.0051c$
Height of the cell at the trailing edge:	$0.0028c$	$5.2 \cdot 10^{-5}c$
# of cells in the laminar b.l. at the L.E.:	1	17
Maximum Δx^+ on the suction side:	550	220
Maximum y^+ on the suction side:	40	0.8
Maximum aspect ratio:	48	440
Maximum i-stretching:	5.9%	6.8%
Maximum j-stretching:	20.7%	14.8%
Size of the computational domain:	$20c \times 20c$	$20c \times 20c$
Grid refinement along the wake:	yes	yes

Table 1: Data on the Chalmers mesh and the Chalmers II mesh.

layer thickness, δ, in the streamwise and spanwise direction, respectively. Since the boundary layer thickness is not expected to change much as the Reynolds number increases, this is an estimation of the required resolution which is fairly independent of this number.

In Fig. 21 spectra on the first and second mesh are shown at a point in the turbulent boundary layer at $x = 0.20c$ (the wall-normal distance is approximately the same, however the resolved energy is quite different on the two meshes). The wave number spectra in the streamwise direction are approximate, constructed from frequency spectra. Especially in the streamwise spectra we see the increased resolution and the cut-off in $-5/3$-range regions. On the coarse mesh we barely resolve the large scales and are far from resolving the smaller scales in the inertial sub range. Also note the high anisotropy in the energy on the coarse mesh, with very low wall-normal stress levels. (A note on how the cut-off values have been decided on the streamwise spectra: according to theory the cut-off should be at $k_x = \pi/\Delta x$, however in the

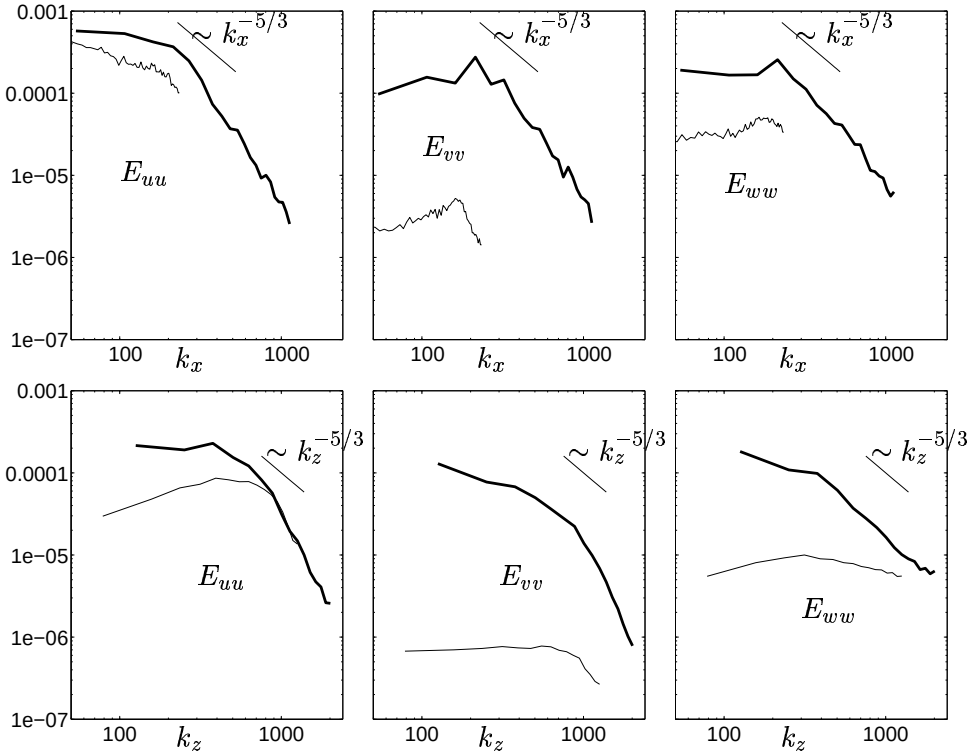

Figure 21: Wave number spectra in the streamwise (approximate) and spanwise direction (top and bottom figures, respectively) at a point at 20% of the chord. Thin lines: Chalmers mesh; thick lines: Chalmers II mesh.

figure the lines have been cut off at $k_x \approx 1/\Delta x$. For higher values the turbulence is not resolved, perhaps since the spectra are approximations from the frequency spectra.) The value of having a resolved flow in the off-near-wall region is investigated in Paper V.

Laminar boundary layer

Figure. 22 shows velocity vectors on the two meshes. From the initial coarse-mesh computations it was seen that the laminar boundary layer was not resolved. In the second mesh (the Chalmers II mesh) this was taken care of, however leading to an increase in the amount of wall-

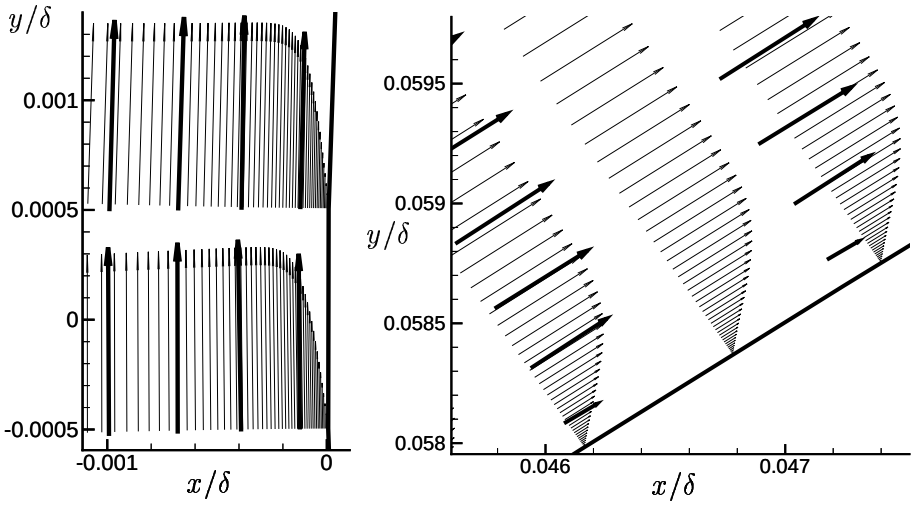

Figure 22: Velocity vectors in the laminar boundary layer. Thick vectors: Chalmers mesh; thin vectors: Chalmers II mesh.

normal nodes (128 nodes). On this mesh, the height of the cell at the leading edge is as small as $5{\cdot}10^{-6}c$. In Fig. 23 contour levels of the velocity in the x-direction are shown. The red lines are from a computation on the coarse mesh and the solid lines are from the finer mesh. A wiggle detector described later in this chapter is used on the Chalmers II mesh simulation (resulting in a scheme that is less dissipative than the second-order van Leer scheme, see Fig. 14 in Paper IV), whereas on the coarse mesh the van Leer scheme is prescribed in the particular region shown in the figure. Although a less dissipative scheme is used, the oscillations present on the coarse mesh do not appear on the mesh with finer resolution.

Transitional bubble

In Fig. 24 a part of the laminar separation bubble is shown. On the coarse mesh only an incipient bubble is present (not seen here, instead see Fig. 13 in Paper III). Figure 24 also shows the increase in the streamwise resolution, necessary in order to capture the transition and the reattachment of the bubble (see also Fig. 5 in Paper IV).

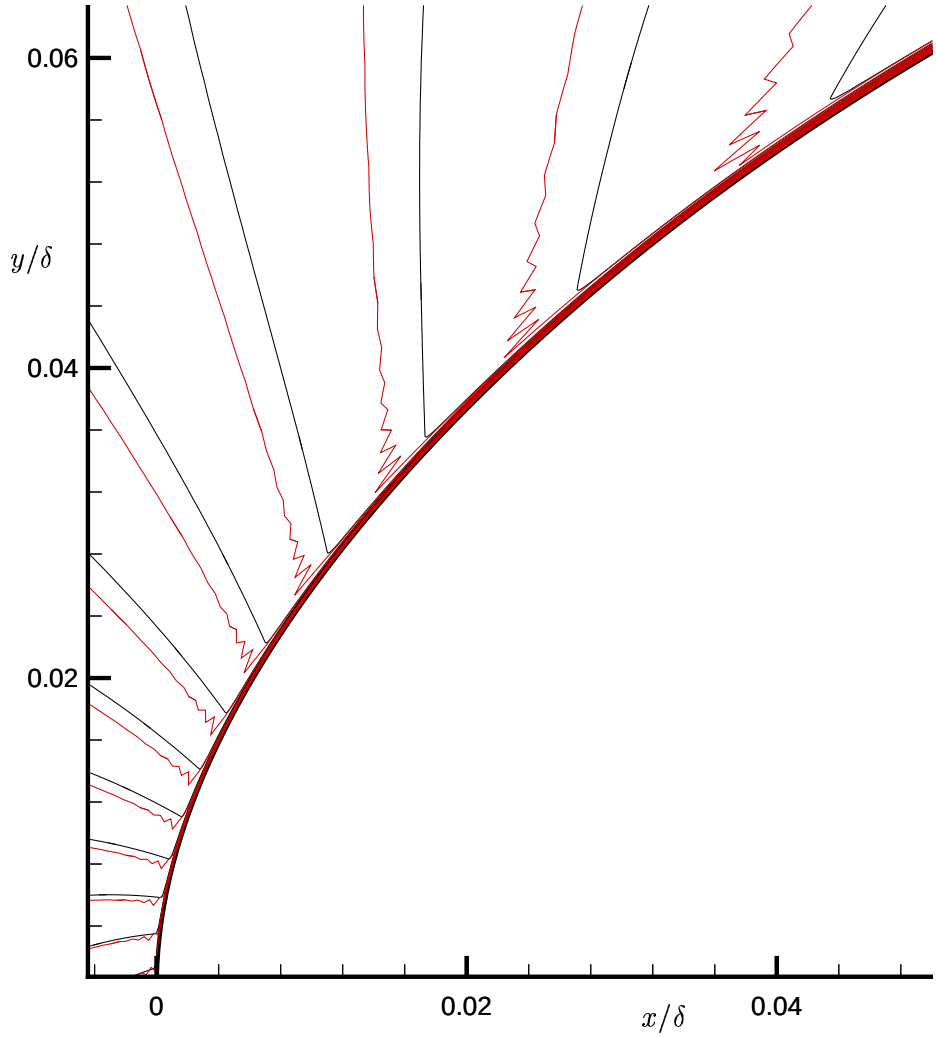

Figure 23: Contour levels of the $\overline{u}$-velocity in the region around the leading edge. Red lines: Chalmers mesh; black lines: Chalmers II mesh.

2D/3D approach

From the computations on the first mesh the boundary layer thickness could be estimated. On the second-iteration mesh this estimate has

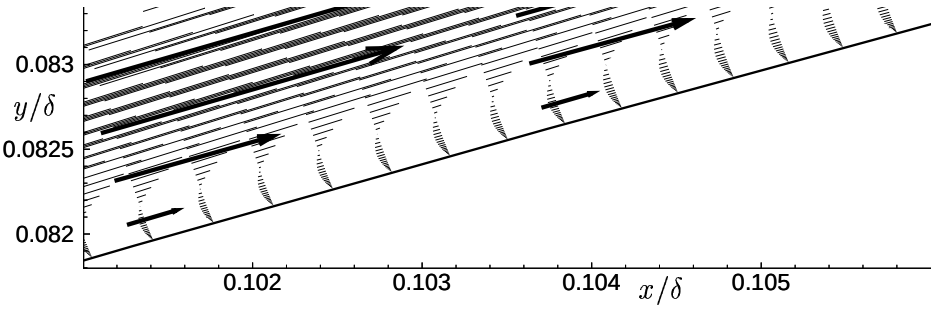

Figure 24: Velocity vectors in the laminar separation region on the Chalmers II mesh (thin vectors) and velocity vectors on the Chalmers mesh (thick vectors).

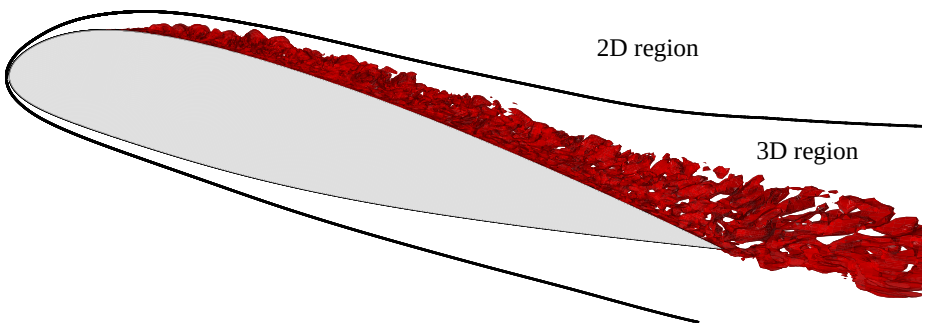

Figure 25: The choice of the 2D/3D interface on the Chalmers II mesh and contour levels of the spanwise velocity (1% of the freestream velocity).

been used to decrease the number of nodes by using a 2D/3D approach. On a sufficient distance outside turbulent regions only 2D simulation is performed (the spanwise amount of nodes is 3). In the 3D region, 33 nodes are used. This 2D/3D approach, which was used by ONERA [21], saves 45% of the nodes. In Fig. 25 the matching line between the 2D region and the 3D region is shown. The turbulent region seems to be dangerously close to the matching line, e.g. at 30% of the chord, however in this particular simulation the boundary layer thickness is overpredicted (see Fig. 11 in Paper IV), much because of a too large transitional separation bubble in the simulations.

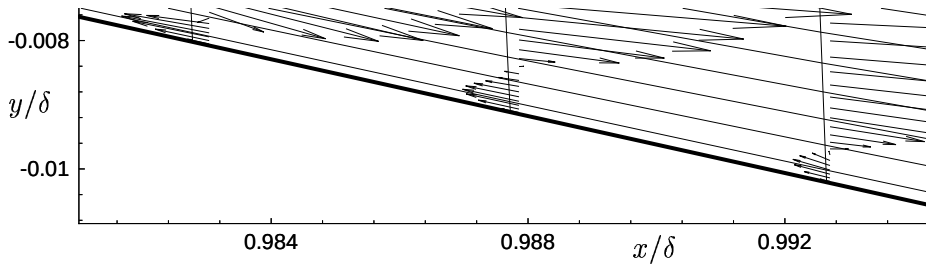

Figure 26: The Chalmers mesh near the trailing edge region and velocity vectors on the Chalmers II mesh.

Trailing edge separation bubble

Figure 26 shows an instantaneous plot of a trailing edge bubble from one simulation on the second-iteration mesh. Also shown is the initial mesh. Note that the difference between the two meshes in this region is only in the resolution in the wall-normal direction. The finer resolution in this direction is needed to be able to capture these very thin trailing edge bubbles that appears (not necessarily in the mean) at this angle of attack.

Handling Unphysical Oscillations

Spatial scheme

The central difference scheme (CDS) is often used in LES because of its non-dissipative and energy-conserving properties. When the momentum equations are discretized in space using this scheme it can produce odd-even oscillations (grid-to-grid oscillations or wiggles) if the resolution is poor. In the present computations, to be able to remove unphysical oscillations, a bounded second-order upwind scheme (the van Leer scheme) is mixed with the CDS. The schemes are blended and the convective flux can be expressed as:

$$\dot{m}u^m_{UDS} + \dot{m}\left[\alpha u^{m-1}_{CDS} - \alpha u^{m-1}_{UDS} + (1-\alpha)u^{m-1}_{UDScorr}\right], \tag{2}$$

for a face in the i-direction. CDS stands for the central difference scheme, UDS for the 1st-order upwind scheme and $UDScorr$ for the 2nd-order correction to the lower order upwind scheme ($m-1$ is the

previous iteration). Here α is a blending factor ($0 \leq \alpha \leq 1$) and, at the extremes, we have:

$\alpha = 0$: the van Leer scheme
$\alpha = 1$: the central difference scheme with deferred correction [22]

Prescribed transition

In the initial computations the second-order upwind scheme of van Leer was used in the laminar region and it was gradually blended to make the CDS active in the turbulent boundary layer. This was used on the Chalmers mesh to prescribe the transition. More details about this approach is found in Paper I and Paper III. This is not an ideal approach, however it might be the only feasible approach when using very coarse meshes.

Wiggle detector

Wiggle detectors were used in the LESFOIL project [21, 23] and here a smooth version, that was used on the Chalmers II mesh, is presented. The wiggle detector checks if a wiggle is present in the i-, j- or k-direction for any of the three velocities. If this is the case the scheme changes 1 % towards the van Leer scheme, i.e. $\alpha^{n+1} = \max(\alpha^n - 0.01, 0)$, where n denotes time step number. Otherwise the scheme is more centred and $\alpha^{n+1} = \min(\alpha^n + 0.01, 1)$.

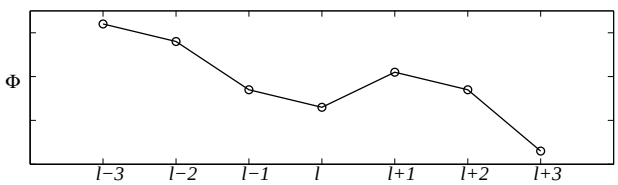

Figure 27: The definition of a wiggle in the computations. In this example there is an unphysical wiggle on face $l + 1/2$, but not on face $l - 1/2$.

It is not obvious what is an unphysical wiggle and what is turbulence. This is one reason for changing the scheme smoothly. Apart from this the wiggle definition is arbitrary and is chosen in order to

minimise the numerical dissipation, without destabilising the numerical procedure. In the computations a wiggle is present in the l-direction ($l = i, j, k$), if the coefficient of direction changes twice from node to node in this direction (see Fig.27). That is, if (for any velocity component Φ)

$$\begin{gathered} (\Phi_{l+1} - \Phi_l)\,(\Phi_l - \Phi_{l-1}) < 0 \\ \text{and} \\ (\Phi_{l+2} - \Phi_{l+1})\,(\Phi_{l+1} - \Phi_l) < 0 \end{gathered} \tag{3}$$

is true, then a wiggle is present and α in the convective flux in Eq. 2 through face $l + 1/2$ is modified ($\alpha^{n+1} = \max(\alpha^n - 0.01, 0)$).

Treatment of the Laminar Region

Because of the strong coupling between the trailing edge separation and the pressure peak at the leading edge, all regions around the airfoil are probably equally important. This is often referred to as a close-to-the-trailing-edge problem although it could be the other way around. It is probably possible to get good agreement with the F2-velocity profiles close to the trailing edge, by using wrong laminar treatments, such as too high freestream turbulence, too dissipative schemes or other doubtful modifications. Of course, something needs to be done in the laminar region, e.g. we would rather have a dissipative scheme than wiggles that contaminate all of the domain. However, it is probably crucial that the treatment in the laminar region is correct.

On the first mesh the van Leer scheme was used in order to remove unphysical oscillations and also in order to prescribe the transition. This is not a satisfactory approach and on the second mesh the wiggle detector is used and there is no prescribing of the transition. These simulations are able to capture the laminar separation bubble and to predict the transition. However, the SGS kinetic energy is not zero in the laminar region. To treat the laminar region in a correct way is probably one of the key issues in order to get quantitatively good results from the airfoil flow simulations.

Parallelisation

The computations have been performed on an IBM SP computer at the Center for Parallel Computing at KTH. The computational domain is

decomposed into 36 subdomains on the second mesh. $4 \times 2 \times 4$ in the 3D domain and $4 \times 1 \times 1$ in the 2D domain. Dirichlet boundary conditions are used between the blocks. More details about the parallelisation can be found in Paper II or Ref. [24].

Numerical Method

The code used is an incompressible finite volume Navier-Stokes solver called CALC-BFC (Davidson and Farhanieh [25]). The solver is based on structured grids and the use of curvi-linear boundary fitted coordinates. A few more details about the code is found in Appendix.

6 NEAR-WALL MODELLING

In a wall-resolved LES the near-wall structures described in Chapter 2 are sufficiently resolved. A wall-resolved LES is not an alternative for high-Reynolds-number flows however, as seen in the next chapter.

In Paper IV, the value of a coarse LES of the flow around the Aerospatiale A-profile is discussed, in which the region outside the near-wall region is sufficiently resolved. The value is probably greater in flows where the near-wall region is less dominant, e.g where curvature effects, separation and transition are present. For example in Paper IV it is argued that the prediction of the transition is more important than the near-wall modelling, in order to get good results on the airfoil flow.

Nevertheless, coarse LES fails to produce accurate results even in channel flows. This seemingly simple flow is actually very demanding for LES. The flow is completely determined by the turbulence in the boundary layers and the small spanwise structures must be resolved in order to achieve accurate results. In the work presented in this thesis attempts have been conducted, using the wall-function approach described below and also to use hybrid approaches, where RANS is used close to the wall.

Wall-Functions

Numerically, when the near-wall resolution is insufficient, the correct value of the wall shear stress ($\tau_{wall} = \mu \left(\partial \overline{u}/\partial y\right)_{wall}$) needs to be determined. The wall shear stress is usually assumed to be correlated to the velocity in the log region through the use of a near-wall law, e.g. the power law, or the log law. In Paper I and III the wall law in Fig. 28 is used. This wall-function and how it is implemented are described in detail in Paper III.

In Fig. 29 velocity profiles are shown for computations where the no-slip condition is used and where the instantaneous wall law shown in Fig. 28 is used for the wall-function. The results are slightly better when the wall-functions are used on this very coarse mesh (the Chalmers mesh in Table 1 on page 20) with $\Delta x^+_{\max} \approx 550$ and $\Delta z^+_{\max} \approx 350$. However, it is clear from Fig. 28 that a wall law such as the log law in the wall-functions around the suction side of an airfoil, is not accurate.

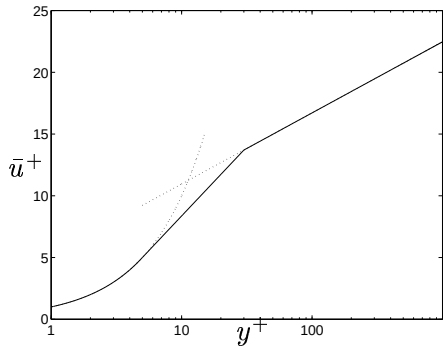

Figure 28: Wall law used in the wall-function computation in Fig. 29

Hybrid RANS/LES

To be able to model the near-wall structures is often referred to as the near-wall problem of LES. In the RANS approach however this problem is not that apparent, since the structures only need to be resolved in the mean, leading to a relaxation on the requirements on the resolution in the streamwise and spanwise directions. The idea with hybrid RANS/LES is to use RANS in the near-wall region, benefitting from the coarser resolution required. In the region outside the near-wall region, in the off-near-wall region, LES is used. In Fig. 30 a RANS-like computation is compared to hybrid RANS/LES, where the matching line between the two methods is placed at $y^+ \approx 43$. Note that in the RANS computation the resolved stresses are almost zero, whereas the stresses increase in the LES region for the hybrid computation. Looking at the eddy viscosity (the bottom figure to the right in Fig. 30), the idea with hybrid RANS/LES is illustrated: when reaching the LES region, the eddy viscosity decreases significantly and thus the modelled shear stress ($\overline{uv}^+_{tot} - \overline{uv}^+_{res}$) becomes low (see bottom figure to the left), resulting in that the resolved stresses increase. However, the standard hybrid RANS/LES approach fails in this channel case, which is described in detail in Paper V.

Hybrid RANS/LES with Interface Condition

From the results with standard hybrid RANS/LES, it seems as if an additional condition is needed at the interface. In Fig. 31 the standard

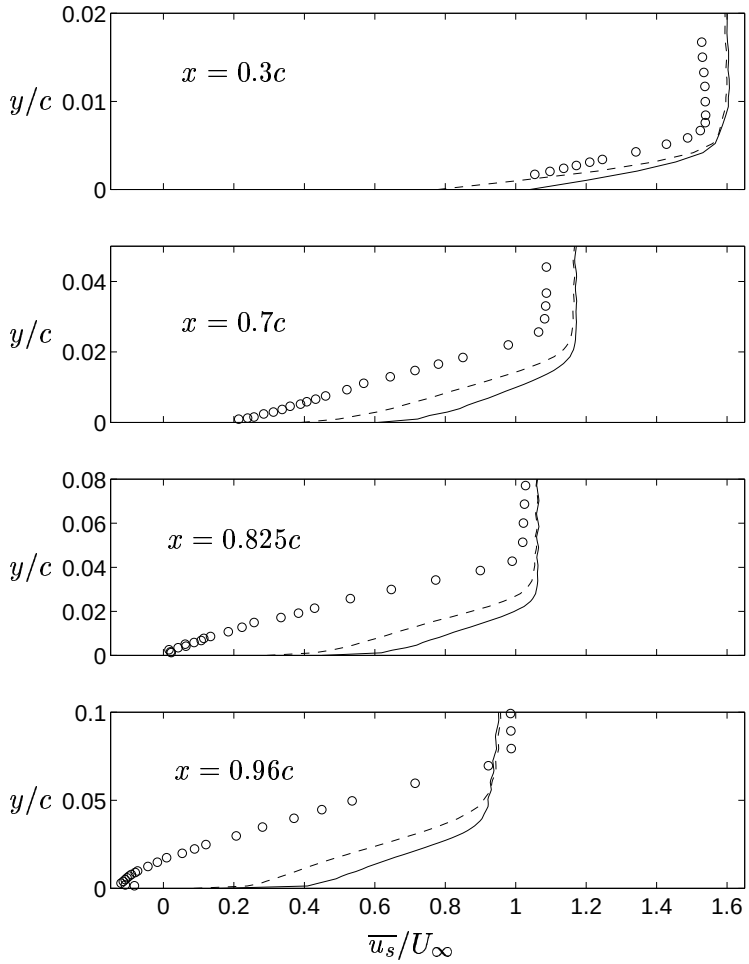

Figure 29: Coarse mesh simulation (on the Chalmers mesh). Spanwise and time averaged streamwise velocity profiles. Solid lines: no-slip wall boundary condition; dashed lines: approximate wall boundary condition from the wall law in Fig. 28; circles: exp. (F2).

hybrid RANS/LES is compared to a hybrid RANS/LES where an interface condition with turbulent structures are used. The interface condition is described in detail in Paper V, where also results from diffuser computations are presented. With this approach there are promising results for the flows in the channel and in the diffuser.

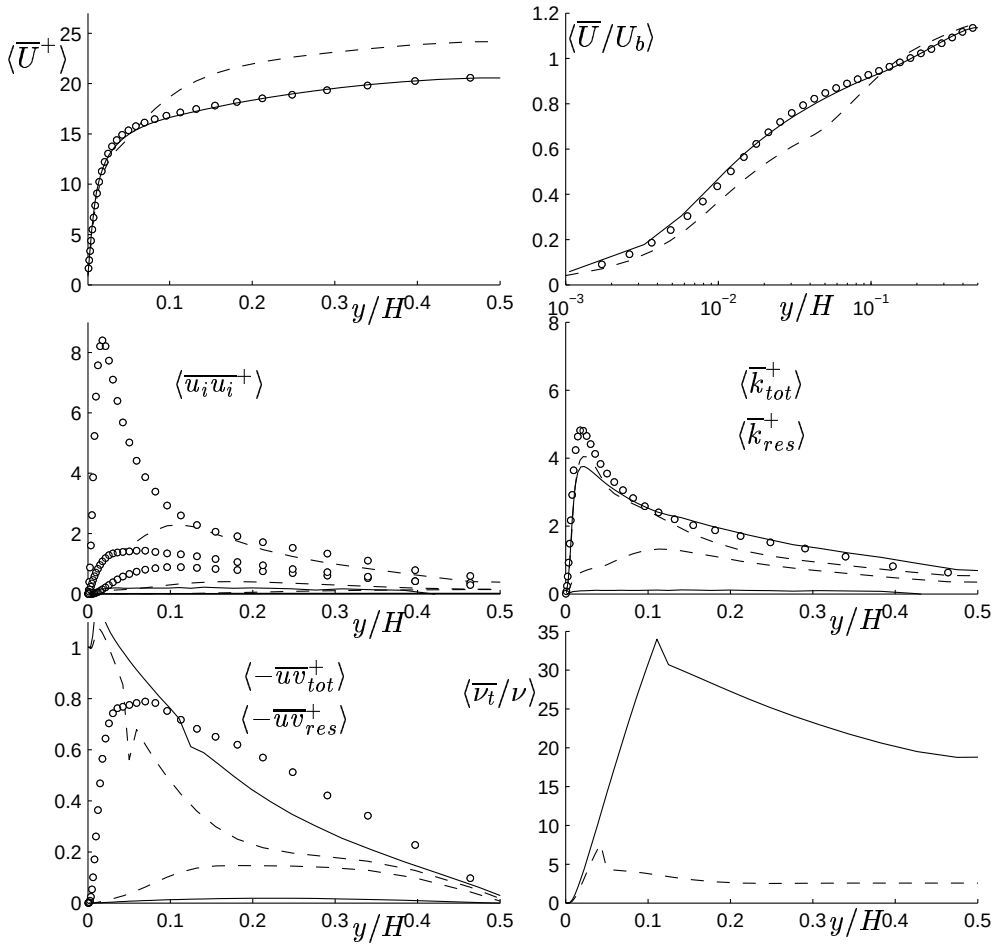

Figure 30: Profiles for the inlet channel case (described in Paper V). Solid lines: RANS-like computation; dashed lines: standard hybrid RANS/LES with matching line at $y^+_{ml} \approx 43$.

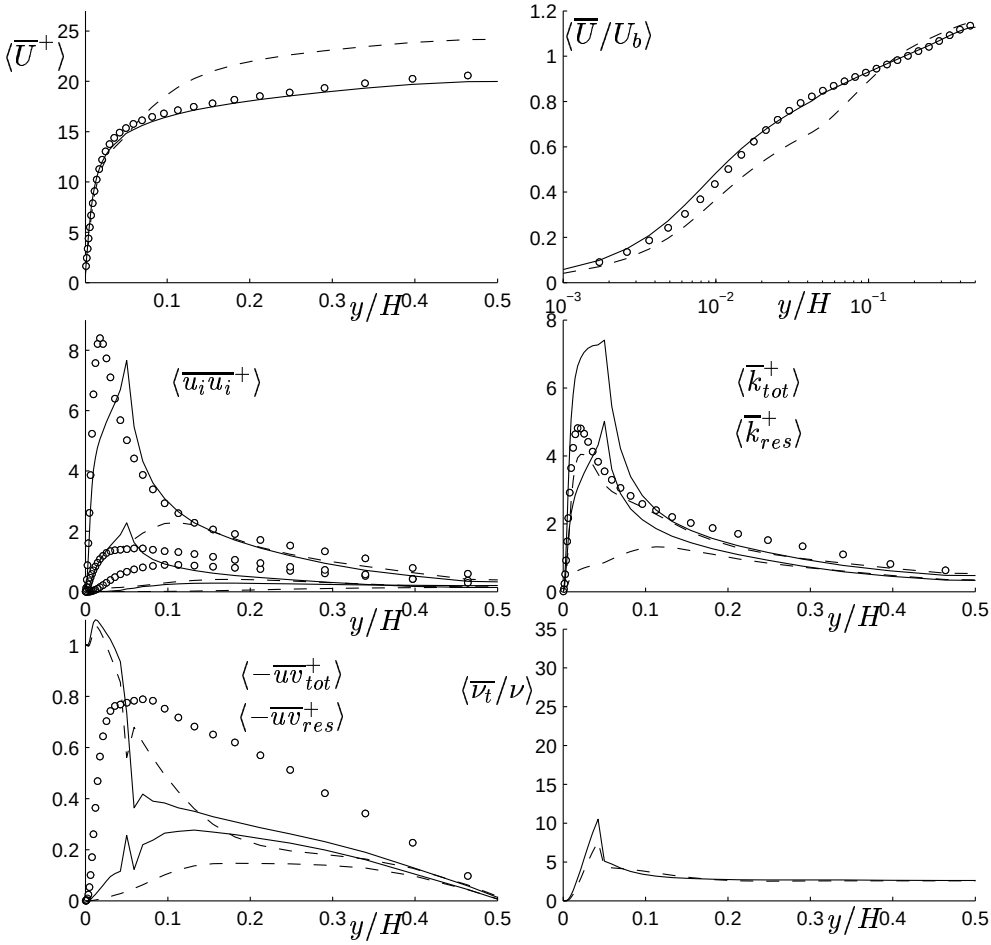

Figure 31: Profiles for the inlet channel case (described in Paper V). Solid lines: hybrid RANS/LES employing interface condition wit turbulent structures; dashed lines: standard hybrid RANS/LES. Matching lines at $y^+_{ml} \approx 43$.

7 ESTIMATION OF REQUIRED RESOLUTION

In this chapter the future of LES is discussed, especially the requirements on LES in order to compute flows around wings. Also the importance of near-wall modelling (such as hybrid RANS/LES) is stressed. In Ref. [26] Spalart estimates the feasibility of different methods and at what year the methods are ready. Here similar estimates are done, however with the coarse simulations presented in this thesis as a base.

Resolution at $Re = 2 \cdot 10^6$

So, what are the characteristics of the present simulations? The mesh consists of 3.2 million nodes, the spanwise distance is 5% of the chord and an averaging time of $10c/U_\infty$ is regarded as sufficient. With a time step of $1 \cdot 10^{-4} c/U_\infty$, the required nodes in space and time is $3.2 \cdot 10^{11}$. Now supposing the present coarse LES approach should be applied on a 3D wing with a span of 8 chords, the total amount of nodes would be 512 million (it is a factor of 160 larger, compared to the present 2D profile with a spanwise distance of $0.05c$). As in Ref. [26], 6 spans of averaging is regarded as necessary for a wing, however the same time step can be used as for the 2D profile and the required nodes in space and time becomes $2.5 \cdot 10^{14}$.

Resolution at Higher Reynolds Numbers

In order to estimate the required resolution when the Reynolds number increases the resolution has to be related to this number. For the amount of nodes in the streamwise and spanwise direction, the following is assumed for an airfoil (with at most incipient separation near the trailing edge and $Re = U_\infty c/\nu$):

$$N_x^{tot} \sim c/\Delta x = \frac{c u_\tau}{\Delta x^+ \nu} \sim \frac{Re^{-0.0695} c U_\infty}{\Delta x^+ \nu} = \frac{Re^{0.9305}}{\Delta x^+} \tag{4}$$

$$N_z^{tot} \sim c/\Delta z = \frac{c u_\tau}{\Delta z^+ \nu} \sim \frac{Re^{-0.0695} c U_\infty}{\Delta z^+ \nu} = \frac{Re^{0.9305}}{\Delta z^+} \tag{5}$$

Here it is assumed that for the friction velocity:

$$u_\tau = \sqrt{\frac{\tau_w}{\rho}} = \sqrt{1/2 c_f} U_\infty \sim \sqrt{1/2 \overline{c}_f} U_\infty \tag{6}$$

where in Eqs. 4-5, as en estimate for an airfoil, the flat plate mean (or total) skin friction coefficient of Nikuradse is used: $\overline{c}_f = 0.02666 Re^{-0.139}$ (taken from Ref. [27]). In the wall-normal direction the number of nodes only has a weak dependence on the Reynolds number (N_y^{tot} is proportional to $\ln(Re)$). Here we assume that N_y^{tot} is independent of the Reynolds number. The CFL number should be constant (and less than one) and the number of time steps, N_t, becomes:

$$N_t \sim \frac{c/U_\infty}{\Delta t} \sim c/\Delta x \sim \frac{Re^{0.9305}}{\Delta x^+} \tag{7}$$

Discussion

The present simulations of the flow around the 2D airfoil are viewed as most feasible (regarding the computing time, not regarding the accuracy) in the year of 2000. This coarse approach is not *ready*, since it lacks accuracy in the modelling of the near-wall region and the treatment of the laminar region. Further, time will tell if it is sufficient with an amount of 8 nodes per boundary layer thickness just downstream of the transition ($N_x \approx N_z \approx 8$), as is the case in the present computations.

Three different roads are marked in Fig. 32:

- Wall-resolved LES with $\Delta x^+ = 50$ and $\Delta z^+ = 20$ just downstream of the transition.
- Wall-function resolution: a resolution of 200 wall units ($\Delta x^+ \approx \Delta z^+ \approx 200$) and 8 nodes per boundary layer thickness downstream of the transition at $Re = 2 \cdot 10^6$.
- Hybrid RANS/LES resolution: $y_1^+ < 1$ and $N_x \approx N_z \approx 8$ downstream of the transition.

The year scale is based on that the computer power increases by a factor of two every second year. If there are requirements on the resolution in wall units, the total amount of nodes in space and time are strongly dependent on the Reynolds number, as seen in the figure. With the estimates above the resolution in space and time scales like $Re^{2.79}$ for wall-resolved LES and the LES with wall-unit requirements on the wall-function resolution. These methods are referred to by Spalart *et*

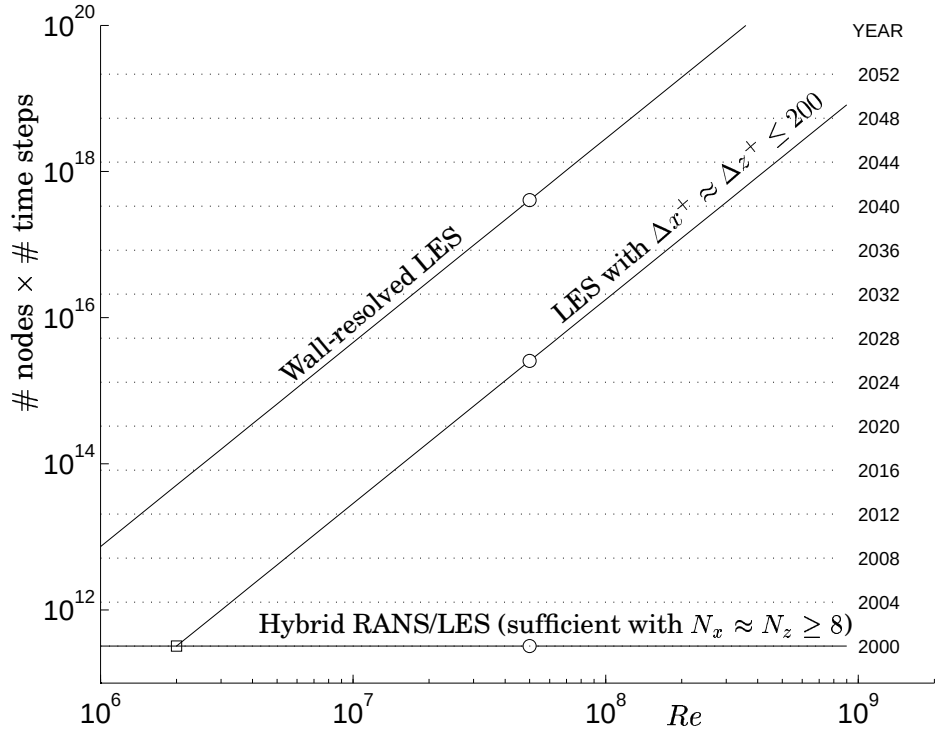

Figure 32: Estimates for 2D wing-profile computations. Square: the present computation; circles: the "real-life" Reynolds number at take-off and landing.

al. as Quasi-DNS (QDNS) methods [4]. If, the near-wall problem is solved, i.e. there are no requirements on the near-wall resolution in wall units, the amount of nodes becomes rather Reynolds independent (if the boundary layer thickness does not increase much). This case is marked with a horizontal line in Fig. 32. As the Reynolds number increases, the crucial difference between this approach and QDNS approaches is illustrated in Fig. 32. The possible road seem to be to use the hybrid RANS/LES approach in order to conduct simulations at the "real-life" Reynolds numbers. Here the resolution only needs to be refined in the wall-normal direction and the number of nodes scales like $\ln(Re)$.

Figure 33 shows the estimations for a 3D wing together with an es-

timate from Ref. [4], where $N_0 = N_x = N_y = N_z = 20$, an unstructured grid is used and the boundary layer is turbulent from the attachment line. This high estimate demonstrates how very thin the boundary layer around the leading edge is. Further, it is assumed that the near-wall problem is solved.

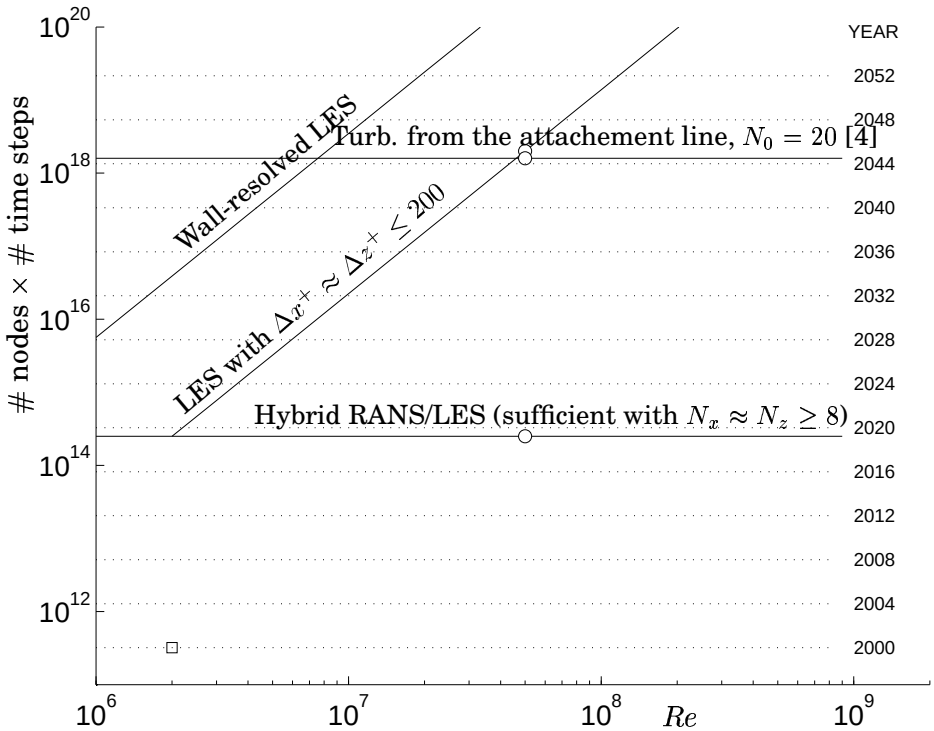

Figure 33: Estimates for 3D wing computations. Square: the present computation; circles: the "real-life" Reynolds number at take-off and landing.

8 SUMMARY OF PAPERS

In this chapter a summary of the papers is given. The main aim with this chapter is not only to summarise the papers but also to relate the papers to each other and highlight conflicting conclusions and statements.

Paper I: Large Eddy Simulation of the Flow Around an Aerospatiale A-Aerofoil

In this paper two meshes were used: the coarse mesh described in Chapter 5, the Chalmers mesh, and also an even coarser mesh consisting of only 690 thousand nodes. In the computations, the transition was prescribed numerically using an upwinding scheme upstream of the transition and the central difference scheme downstream. The two schemes were blended in the transition region. In the transition region the stresses should peak, however in these simulations on these coarse meshes they are far too anisotropic and we were not able to prescribe the transition accurately. On the very coarse mesh it was demonstrated how upwinding in the region around the leading edge, dampens, not only the unphysical oscillations in this region, but also those otherwise present in the flow downstream of the transition. This paper was the first step in the resolution iteration process (described in Chapter 5), where especially the coarse resolution in the laminar region was stressed. It was found that the wall-function computation gives better results compared to when the no-slip condition is used. Also, for computation # 2, on the very coarse mesh, it was argued that the finer resolution the spanwise direction ($L_z = 0.03c$) is the cause for the similar results as for the wall-function computation on the Chalmers mesh. However, in light of later conclusions, the reason is probably fortuitous and due to the way the transition was treated.

In the paper it was stated, that in order to do a useful LES when wall-functions are used, the streamwise resolution should be less than 600. However, this does not apply on this flow around the airfoil, since the number of nodes per boundary layer thickness is too small. Later work suggests that the resolution should be less than 200 wall units and on the Chalmers II mesh, at least 8 nodes per boundary layer thickness is used. The constant, D, in the wall law that was used in

the computations (Eq. 3), is equal to $5 - \ln 5/C$.

Paper II: Parallel Multiblock CFD Computations Applied to Industrial Cases

In this paper the parallel code that we use is described in detail. Parallel aspects of computations from two different research areas and an academic test case are presented. The paper shows that the parallel efficiency is excellent.

Here it is written that a 2 million nodes mesh is a sufficient wall-function mesh, whereas we now know that it is not and hope is that the Chalmers II mesh gives the required wall-function or hybrid RANS/LES resolution. That is, that a resolution less than 200 wall units and/or that 8 nodes per boundary layer thickness are sufficient.

Paper III: Large Eddy Simulation of the Flow Around an Airfoil

Two computations on the Chalmers mesh were presented in this paper, using the Smagorinsky SGS model and the one-equation SGS model by Yoshizawa. In this paper (as in Paper I), the boundary layer was tripped numerically and also here we were not able to prescribe the transition correctly: the transition either took place too far downstream or it was too anisotropic and unphysical. In this paper spectra are used to show the coarse resolution in the off-near-wall region.

Here the spanwise distance was set to $L_z = 0.12c$. It is probably not necessary to use this wide distance in this mainly attached flow. In comparison, the wall-resolved LES in Ref. [21] used $L_z = 0.015c$, the simulations presented in Paper I used $L_z = 0.08c$ and $L_z = 0.03c$ and the simulations presented in Paper IV used $L_z = 0.05c$. In Paper III as well as in Paper I, the velocity profiles were compared to the experiments in the F2 wind tunnel. It was stated that the computations fail in predicting the trailing edge separation bubble. What we should note is that the trailing edge separation is weaker in the F1 wind-tunnel experiments.

Paper IV: Large Eddy Simulation Applied to a High-Reynolds Flow Around an Airfoil Close to Stall

In this paper the one-equations SGS model by Yoshizawa was used on the second-iteration mesh, the Chalmers II mesh. In the simulations a wiggle detector and a 2D/3D approach were used. The wiggle detector worked fine and here the transition was predicted, however the laminar separation bubble was too large and it was concluded that the treatment of the laminar and transitional regions need further investigations. The two computations presented in the paper differ only in the treatment of the laminar region and it was shown that this has a major influence on the turbulent boundary layer further downstream.

Paper V: Hybrid RANS/LES employing Interface Condition with Turbulent Structure

In this paper hybrid RANS/LES methods were applied to an asymmetric diffuser and its inlet channel. Varying the filter width in the LES region and the extent of the RANS domain, these results showed good results only when the model was shifted towards RANS. It was concluded that the usual hybrid RANS/LES approach with a switch from RANS to LES at a matching line does not work. Employing turbulent structures from the inlet data (i.e. DNS data from plane channel simulations) as additional conditions at the interface, good results were obtained for the inlet channel case and the diffuser.

APPENDIX

Governing Equations

Mathematical formulation of Large Eddy Simulation

In LES, the large eddies are solved and the small scales are modelled. Mathematically, the governing equations are filtered by applying the *filter operator*, G, to the equations. The filter operator is defined as:

$$Gf \equiv \overline{f} = \int G(\mathbf{x}, \mathbf{x}', \Delta(\mathbf{x})) f(\mathbf{x}') d\mathbf{x}'$$

where $G(\mathbf{x}, \mathbf{x}', \Delta(\mathbf{x}))$ is the *filter function* and Δ is the *filter width*. An example of a filter function (used in the present work) is the box filter, defined in one dimension as

$$G(x, x') = \begin{cases} 1/\Delta & , \; x - \Delta/2 < x' < x + \Delta/2 \\ 0 & , \; \text{otherwise} \end{cases} . \tag{8}$$

Filtering of the incompressible continuity and momentum equations results in

$$\frac{\partial \overline{u}_i}{\partial x_i} = 0 \tag{9}$$

$$\frac{\partial \overline{u}_i}{\partial t} + \frac{\partial}{\partial x_j}(\overline{u}_i \overline{u}_j) = -\frac{1}{\rho}\frac{\partial \overline{p}}{\partial x_i} + \frac{\partial}{\partial x_j}\left[\nu \frac{\partial \overline{u}_i}{\partial x_j} - \tau_{ij}\right] \tag{10}$$

where

$$\tau_{ij} = \overline{u_i u_j} - \overline{u}_i \overline{u}_j \tag{11}$$

are the subgrid stresses, which are unknown and must be modelled.

In this derivation of the filtered equations, it has been assumed that the filter operator commutes with the spatial derivatives. This is not true for all filter functions, $G(\mathbf{x}, \mathbf{x}', \Delta(\mathbf{x}))$ (as pointed out in e.g. [28]), because, in one dimension, the following integral identity is valid:

$$\int \frac{\partial f(x')}{\partial x'} G(x, x', \Delta(x)) dx' = \frac{d}{dx} \int f(x') G(x, x', \Delta(x)) dx' +$$

$$\int -f(x') \left[\frac{\partial}{\partial x'} G(x, x', \Delta(x)) + \frac{\partial}{\partial x} G(x, x', \Delta(x))\right] dx'$$

i.e. $GDf = DGf + R$, where R is the commutation error and D is the spatial derivative operator. It is clearly seen that the commutation error is zero for those functions that satisfy the following condition:

$$\frac{\partial}{\partial x'}G(x,x',\Delta(x)) = -\frac{\partial}{\partial x}G(x,x',\Delta(x)) \tag{12}$$

The functions that satisfy this condition are of the convolution type, $G(x,x',\Delta(x)) = G(x-x',\Delta(x) = \text{constant})$, i.e. they depend only on $x - x'$. Note also that $\Delta(x)$ must be constant.

The filter width, Δ, is often the same as the grid size and since the grid is refined, e.g. close to walls, this leads to a commutation error in most computations, since then $\partial\Delta/\partial x \neq 0$.

Reynolds Averaged Navier Stokes formulation

Time averaging of the incompressible continuity and momentum equations results in

$$\frac{\partial \overline{u}_i}{\partial x_i} = 0 \tag{13}$$

$$\frac{\partial \overline{u}_i}{\partial t} + \frac{\partial}{\partial x_j}(\overline{u}_i\overline{u}_j) = -\frac{1}{\rho}\frac{\partial \overline{p}}{\partial x_i} + \frac{\partial}{\partial x_j}\left[\nu\frac{\partial \overline{u}_i}{\partial x_j} - \tau_{ij}\right] \tag{14}$$

where here the bar means time averaging. Here τ_{ij} is the turbulence stress term. Note that the equations look exactly the same as the LES equations (Eqs. 9 and 10).

Models

Eddy viscosity hypothesis

The eddy viscosity, ν_T, computed by the models, is related to the unknown stress term, τ_{ij}, using the Eddy viscosity assumption, expressed as

$$\tau_{ij} - \frac{1}{3}\delta_{ij}\tau_{kk} = -2\nu_T\overline{S}_{ij}, \tag{15}$$

where $\overline{S}_{ij} = \frac{1}{2}\left(\frac{\partial \overline{u}_i}{dx_j} + \frac{\partial \overline{u}_j}{dx_i}\right)$ is the strain rate (filtered in the LES sense and time averaged in the RANS sense).

Smagorinsky subgrid scale model

The subgrid scale stresses (11) are the contribution of the small scales, the unresolved stresses. They are unknown and must be modelled. The scales are of the order of the filter width, Δ, and by using mixing length theory, the eddy viscosity, ν_T, is modelled according to Smagorinsky [29] as:

$$\nu_T = (C_S \Delta)^2 |\overline{S}|, \tag{16}$$

where $|\overline{S}| = \sqrt{2\overline{S}_{ij}\overline{S}_{ij}}$. The constant, C_S, is set to 0.1.

Since the Smagorinsky model is an eddy viscosity model, there is an assumption of isotropy for the unresolved scales, which means that the turbulence is in local equilibrium. The SGS kinetic energy equation then reads

$$-\tau_{ij}\overline{S}_{ij} = \text{dissipation} , \tag{17}$$

where the production term, $-\tau_{ij}\overline{S}_{ij}$, acts as a dissipation term in the resolved kinetic energy equation (see [3]). This illustrates the main task of an SGS model: to dissipate the correct amount of energy from the resolved scales acting through the *subgrid scale dissipation*, $\varepsilon_{sgs} = \tau_{ij}\overline{S}_{ij}$.

Yoshizawa's one-equation subgrid scale model

In Yoshizawa's one-equation SGS model [30], the transport equation for the kinetic energy of the unresolved stresses ($k_T = k_{sgs}$), reads:

$$\frac{\partial k_T}{\partial t} + \frac{\partial}{\partial x_j}(\bar{u}_j k_T) = \frac{\partial}{\partial x_j}\left[(\nu + \nu_T)\frac{\partial k_T}{\partial x_j}\right] + P_k - C_\varepsilon \frac{k_T^{3/2}}{\ell_\varepsilon} \tag{18}$$

$$P_k = 2\nu_T \bar{S}_{ij}\bar{S}_{ij}, \;\; \nu_T = C_k \ell_k k_T^{1/2} \tag{19}$$

The constants are [31]: $C_\varepsilon = 1.05$, $C_k = 0.07$ and $\ell_\varepsilon = \ell_k = \Delta$.

Chen & Patel one-equation RANS model

The one-equation turbulence model by Chen and Patel [32] is a model for the turbulent kinetic energy ($k_T = k$). It reads exactly as the one-equation model above (Eqs. 18 and 19), however the constants differ: $C_\varepsilon = 1$, $C_k = 0.09$, $\ell_\varepsilon = 2.495 \cdot y(1 - e^{-0.2y\sqrt{k}/\nu})$ and $\ell_k = 2.495 \cdot y(1 - e^{-0.0143y\sqrt{k}/\nu})$, where y is the distance to the wall.

Numerical Method

The code used is an incompressible finite volume Navier-Stokes solver called CALC-BFC (Davidson and Farhanieh [25]). The solver is based on structured grids and the use of curvi-linear boundary fitted coordinates. The grid arrangement is collocated, and the Rhie and Chow interpolation method [33] is used. The code is parallelised for 3D flows [24] using block decomposition and the message passing systems PVM and MPI. The PISO algorithm is used for the pressure-velocity coupling. The filtered momentum equations (Eqs. 10) are discretized in time using the Crank-Nicolson scheme and in space using 2nd order difference schemes (the central difference scheme (CDS) and the van Leer scheme).

In Paper V an incompressible, finite volume code is used [34]. For space discretization, central differencing is used for all terms. The Crank-Nicolson scheme is used for time discretization. The numerical procedure is based on an implicit, fractional step technique with a multigrid pressure Poisson solver and a non-staggered grid arrangement [35].

References

[1] S.J. Kline, W.C. Reynolds, F.A. Schraub, and P.W. Runstadler. The structure of turbulent boundary layers. *Journal of Fluid Mechanics*, 30:741–773, 1967.

[2] S.G. Saddoughi and S.V. Veeravalli. Local isotropy in turbulent boundary layers at high Reynolds number. *Journal of Fluid Mechanics*, 268:333–372, 1994.

[3] U. Piomelli and J.R. Chasnov. Large-eddy simulations: Theory and applications. In D. Henningson, M. Hallbäck, H. Alfredsson, and A. Johansson, editors, *Transition and Turbulence Modelling*, pages 269–336, Dordrecht, 1996. Kluwer Academic Publishers.

[4] P.R. Spalart, W-H. Jou, M. Strelets, and S.R. Allmaras. Comments on the feasibility of LES for wings, and on a hybrid RANS/LES approach. 1st AFOSR Int. Conf. on DNS/LES, Aug. 4-8, 1997, Ruston, LA. In *Advances in DNS/LES, C. Liu & Z. Liu Eds., Greyden Press, Columbus, OH*, 1997.

[5] M. Shur, P. R. Spalart, M. Strelets, and A. Travin. Detached-eddy simulation of an airfoil at high angle of attack. In W. Rodi and D. Laurence, editors, *Engineering Turbulence Modelling and Experiments 4*, pages 669–678. Elsevier Science, 1999.

[6] N. V. Nikitin, F. Nicoud, B. Wasistho, K. D. Squires, and P. R. Spalart. An approach to wall modeling in large-eddy simulations. *Physics of Fluids*, 12:1629–1632, 2000.

[7] M. Strelets. Detached eddy simulation of massively separated flows. 39th Aerospace Sciences Meeting, AIAA Paper 2001-0879, Reno, 2001.

[8] L. Davidson, D. Cokljat, J. Fröhlich, M. Leschziner, C. Mellen, and W. Rodi, editors. *LESFOIL- Large Eddy Simulation of Flow Around a High-Lift Airfoil*. Springer, 2002. In print.

[9] E. Chaput. Aerospatiale-A Airfoil. Contribution in ECARP- European Computational Aerodynamics Research Project: Validation of CFD Codes and Assessment of Turbulence Models. In W. Haase

*e*t al., editor, *Notes on Numerical Fluid Mechanics*, volume 58, pages 327–346. Vieweg Verlag, 1997.

[10] October issue of Flyer, 1997.

[11] 26 October - 1 November issue of Flight International, 1994.

[12] W. Haase, F. Brandsma, E. Elsholz, M. Leschziner, and D. Schwamborn, editors. *EUROVAL- A European Initiative on Validation of CFD-codes*, volume 42. Vieweg Verlag, 1993.

[13] W. Haase, E. Chaput, E. Elsholz, M. Leschziner, and U. Müller, editors. *ECARP- European Computational Aerodynamics Research Project: Validation of CFD Codes and Assessment of Turbulence Models*, volume 58. Vieweg Verlag, 1997.

[14] L. Davidson and A. Rizzi. Navier-Stokes stall predictions using an algebraic stress model. *J. Spacecraft and Rockets*, 29:794–800, 1992.

[15] L. Davidson. Prediction of the flow around an airfoil using a Reynolds stress transport model. *ASME: Journal of Fluids Engineering*, 117:50–57, 1995.

[16] F.S. Lien and M.A. Leschziner. Modelling of 2D separation from high-lift aerofoils with a non-linear eddy-viscosity model and second-moment closure. *The Aeronautical Journal*, 99:125–144, 1995.

[17] H.-J. Kaltenbach and H. Choi. Large-eddy simulation of flow around an airfoil on a structured mesh. In *Annual Research Briefs 1995*, pages 51–60, Center for Turbulent Research, Stanford Univ./NASA Ames Reseach Center, 1995.

[18] C. Weber and F. Ducros. Large-eddy and reynolds averaged navier-stokes simulations of turbulent flow over an airfoil. *Int. J. Comput. Fluid Dyn.*, 13:327–355, 2000.

[19] J. Held. *Large Eddy Simulation of Separated Compressible Flows around Wing Sections*. PhD thesis, Dept. of Heat and Power Engineering, Lund Institute of Technology, Lund, 1999.

[20] P. E. Morgan and M. R. Visbal. Large-eddy simulation of airfoil flows. 41st Aerospace Sciences Meeting, AIAA Paper 2003-0777, Reno, 2003.

[21] I. Mary and P. Sagaut. Large Eddy Simulation of flow around an airfoil near stall. *AIAA Journal*, 40(6):1139–1145, 2002.

[22] J.H. Ferziger and M. Peric. *Computational Methods for Fluid Dynamics*. Springer-Verlag, Berlin, 1996.

[23] F. Ducros. Contribution by CERFACS in LESFOIL- Large Eddy Simulation of Flow Around a High-Lift Airfoil. In L. Davidson, D. Cokljat, J. Fröhlich, M. Leschziner, C. Mellen, and W. Rodi, editors, *LESFOIL*. Springer, 2002. In preparation.

[24] H. Nilsson and L. Davidson. CALC-PVM: A parallel multiblock SIMPLE multiblock solver for turbulent flow in complex domains. Technical Report 98/12, Dept. of Thermo and Fluid Dynamics, Chalmers University of Technology, Gothenburg, 1998.

[25] L. Davidson and B. Farhanieh. CALC-BFC: A finite-volume code employing collocated variable arrangement and cartesian velocity components for computation of fluid flow and heat transfer in complex three-dimensional geometries. Rept. 95/11, Dept. of Thermo and Fluid Dynamics, Chalmers University of Technology, Gothenburg, 1995.

[26] P. R. Spalart. Strategies for turbulence modelling and simulations. *Int. J. Heat and Fluid Flow*, 21:252–263, 2000.

[27] H. Schlichting. *Boundary Layer Theory*. McGraw-Hill, Inc., 1979.

[28] P. Moin and J. Jimenez. Large eddy simulation of complex turbulent flows. 24th AIAA Fluid Dynamics Conference, AIAA Paper 93-3099, Orlando, 1993.

[29] J. Smagorinsky. General circulation experiments with the primitive equations. *Monthly Weather Review*, 91:99–165, 1963.

[30] A. Yoshizawa. Statistical theory for compressible shear flows with the application of subgrid modelling. *Physics of Fluids A*, 29:2152–2163, 1986.

[31] C. Fureby. Large eddy simulation of rearward-facing step flow. *AIAA Journal*, 37(11):1401–1410, 1999.

[32] H.C. Chen and V.C. Patel. Near-wall turbulence models for complex flows including separation. *AIAA Journal*, 26:641–648, 1988.

[33] C.M. Rhie and W.L. Chow. Numerical study of the turbulent flow past an airfoil with trailing edge separation. *AIAA Journal*, 21:1525–1532, 1983.

[34] L. Davidson. Hybrid LES-RANS: A combination of a one-equation SGS model and a $k-\omega$ model for predicting recirculating flows. In *ECCOMAS CFD Conference*, Swansea, U.K., 2001.

[35] P. Emvin. *The Full Multigrid Method Applied to Turbulent Flow in Ventilated Enclosures Using Structured and Unstructured Grids*. PhD thesis, Dept. of Thermo and Fluid Dynamics, Chalmers University of Technology, Gothenburg, 1997.